Electron Holography Image Simulation of Nanoparticles

Keimpema, K.; Raedt, H. De; Hosson, J.Th.M. De

Published in:
Journal of Computational and Theoretical Nanoscience

Publication date:
2006

Electron Holography Image Simulation of Nanoparticles

K. Keimpema,[1,*] H. De Raedt,[1,†] and J.Th.M. De Hosson[1,‡]

[1] *Department of Applied Physics, Materials Science Centre, University of Groningen, Nijenborgh 4, NL-9747 AG Groningen, The Netherlands*

We discuss a real-space and a Fourier-space technique to compute numerically, the phase images observed by electron holography of nanoscale particles. An assessment of the applicability and accuracy of these techniques is made by calculating numerical results for simple geometries for which analytical solutions are available. We employ the numerical techniques to compute the electron holography phase images of slabs with surface roughness and slabs containing magnetic domain walls.

Keywords: Electron holography; Image simulation

I. INTRODUCTION

Already in 1949, Denis Gabor introduced the idea of holography for electron microscopy[1]. However it would take until the end of the 20th centuries before the technique would become implemented in condensed matter physics. The early holograms were limited to the brightness and to the coherence of the filament sources. The development of the field emission gun (FEG), which gives a high intensity, coherent beam, contributed greatly to the implementation of electron holography in practice. Nowadays FEG has been used in almost all electron holography applications. Electron holography is based on recording an interference pattern from which both the amplitude and phase of an object can be reconstructed[2]. There are various electron holographic techniques[3], but one of the most popular is off-axis holography.

In off-axis electron holography, a specimen is chosen that does not completely fill the image plane (for example a small magnetic element or the edge of an extended film) so that only part of the electron beam passes through the specimen. An electrostatic biprism, a thin ($< 1\mu$m) metallic wire or quartz fiber coated with gold or platinum, is used to recombine the specimen beam and the reference beam so that they interfere and form a hologram. This can be digitized and digital image-processing techniques can be applied to reconstruct an image of the magnetic domain structure. Figure 1 shows a ray diagram of the electron beams in holographic mode. The reference beam is assumed to be a plane wave

$$\psi_r(\mathbf{r}) = e^{i2\pi\mathbf{q}\cdot\mathbf{r}}. \tag{1}$$

As a result of the interaction the object beam with the sample, the wave emerging from the object is given by

$$\psi_o(\mathbf{r}) = A_o(\mathbf{r})e^{i\phi_o(\mathbf{r})}, \tag{2}$$

where $A_o(\mathbf{r})$ and $\phi_o(\mathbf{r})$ are the amplitude and phase, respectively. After passing the biprism, the two beams interfere at the image plane

$$I(\mathbf{r},\mathbf{t}) = |\psi_r + \psi_o|^2 = 1 + A_o(\mathbf{r})^2 + 2A_o(\mathbf{r})\cos(2\pi\mathbf{q}\cdot\mathbf{r} - \phi_o(\mathbf{r})), \tag{3}$$

forming the hologram. Clearly, the recorded image $I(\mathbf{r},\mathbf{t})$ contains information about both the phase and the amplitude of the object beam. The image can be reconstructed from the hologram by taking the Fourier transform of Eq.(3):

$$\mathcal{F}(I(\mathbf{t})) = \delta(\mathbf{k}) + \mathcal{F}(A_o(\mathbf{r})^2) + \delta(\mathbf{k}+\mathbf{q}) * \mathcal{F}(A_o(\mathbf{r})e^{i\phi_o(\mathbf{r})}) + \delta(\mathbf{k}-\mathbf{q}) * \mathcal{F}(A_o(\mathbf{r})e^{-i\phi_o(\mathbf{r})}) \tag{4}$$

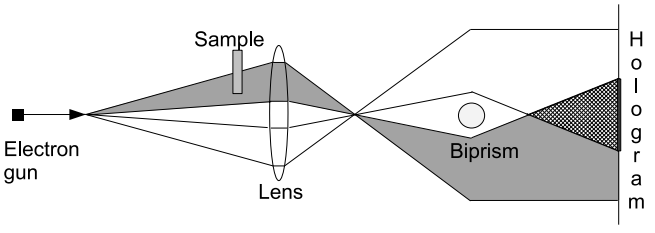

FIG. 1: Typical off-axis configuration used in electron holography.

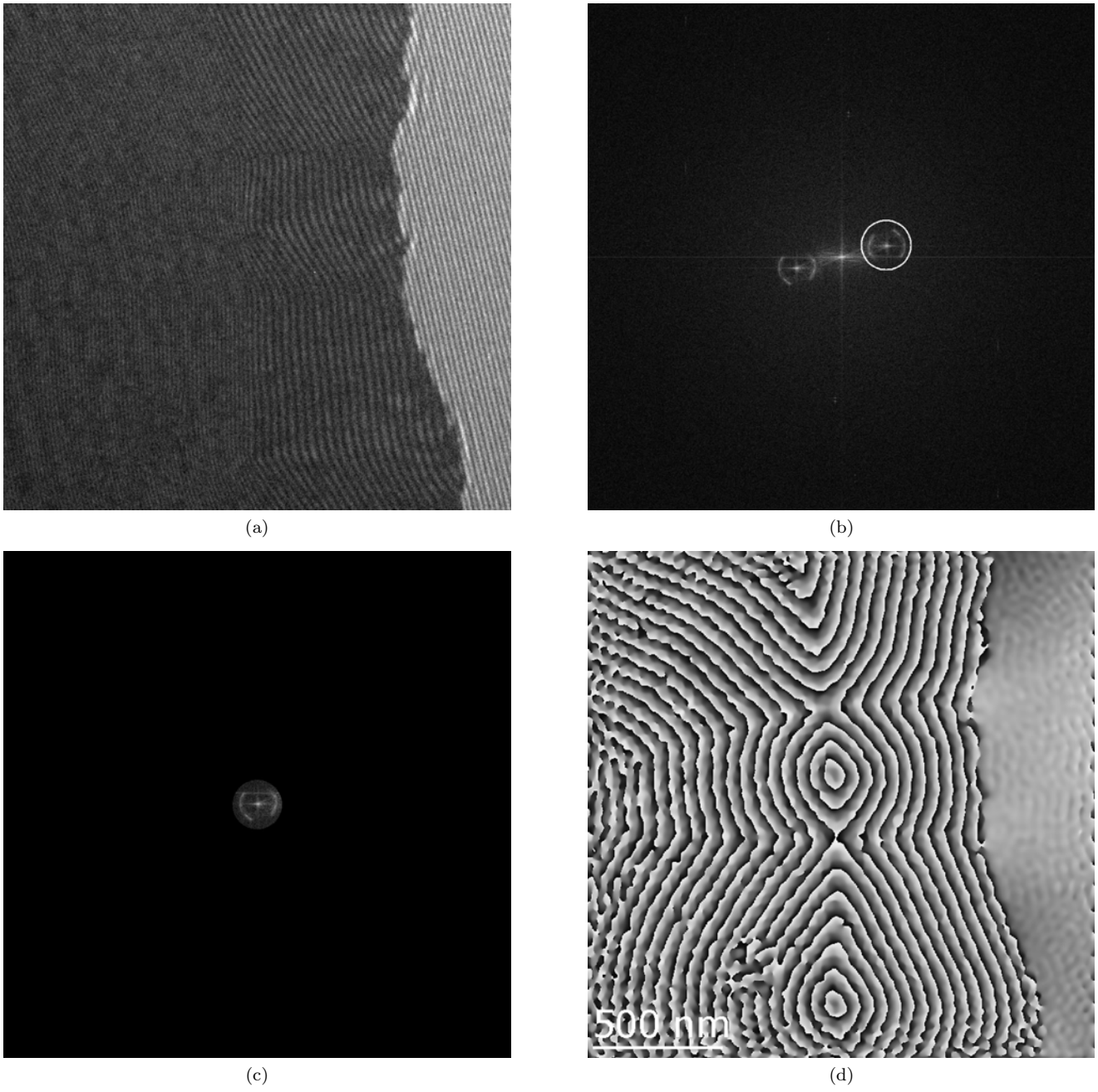

(a) (b) (c) (d)

FIG. 2: Step-by-step procedure to reconstruct the phase from an electron hologram of nanocrystaline $Fe_94N_5Zr_1$. (a): hologram; (b): power spectrum with two side bands; (c): one side band becomes centered; (d): inverse Fourier transform and phase map $\phi_o(x, y) = \arctan(\mathcal{I}/\mathcal{R})$ where $\mathcal{R}$ and $\mathcal{I}$ are the real and imaginary part of the inverse FFT, respectively.

The four terms of Eq.(4) can be interpreted as follows: The first term is the contribution of electrons that propagate through the system without being affected by the sample. The second term yields the intensity, that is, the image obtained by conventional electron microscopy. The third term is the object wave centered around $\mathbf{k} = -\mathbf{q}$. The last term is the complex conjugate of the object wave centered around $\mathbf{k} = \mathbf{q}$.

The phase and amplitude can be numerical reconstructed following the following procedure, illustrated in Fig. 2. First the fast Fourier transformation (FFT) of the holographic image is taken. In frequency domain two sidebands can be detected. If one of the two side bands of the FFT is cut out and centered and the inverse FFT of this centered sideband is taken the phase and amplitude can be calculated using the formulas: $\phi_o(\mathbf{r}) = \arctan(\mathcal{I}/\mathcal{R})$ and $A_o(\mathbf{r}) = (\mathcal{R}^2 + \mathcal{I}^2)^{1/2}$, where $\mathcal{R}$ and $\mathcal{I}$ are the real and imaginary part of the inverse FFT, respectively[4]. Because one of the off-axis sidebands is centered to obtain the phase information the method is called off-axis holography.

The final result of the procedure, sketched above, is a image of the amplitude $A_o(\mathbf{r})$ and phase $\phi_o(\mathbf{r})$. Evidently, the main question is how these images relate to the electrical and/or magnetic properties of the sample. If neither the magnetic flux $\mathbf{B}$ or the crystal potential V vary with depth and neglecting magnetic and electric fields outside the sample, the phase $\phi(x,y)$ in the image plane is given by an electric contribution $\phi_e(x,y)$ and a magnetic contribution $\phi_m(x,y)$

$$\phi_o(x,y) \;=\; \phi_e(x,y) + \phi_m(x,y) = C_E V(x,y) l_z(x,y) - \frac{e}{\hbar}\int_S \int B_\perp(x,y) l_z(x,y) dxdy, \tag{5}$$

where C_E is a constant, $l_z(x,y)$ is the thickness as function of position in the (x,y)-plane and $B_\perp$ denotes the component of the magnetic induction perpendicular to both x and the direction of electron beam propagation z. Assuming that the thickness is constant over the whole image and that the composition is homogeneous, the first right-hand side term is a constant and only the second term remains. If the phase is recovered, the derivative of the phase, multiplied by a constant, will give the magnetic induction in the x- and y-direction as function of the position in the holographic image.

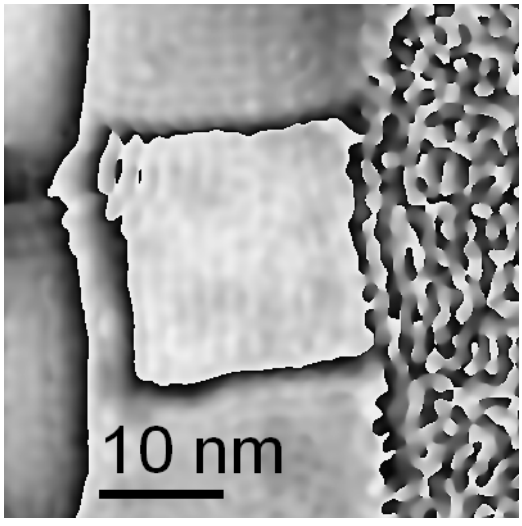

FIG. 3: Phase change within a Mo cluster of a size 20 nm lying on a Si_3N_4 membrane, reconstructed from an electron hologram demonstrating nearly constant thickness in projected direction. The hologram taken at a biprism voltage adjusted to give 0.5 nm fringes, was recorded on a 1k x 1k Gatan multiscan 794IF CCD camera[5].

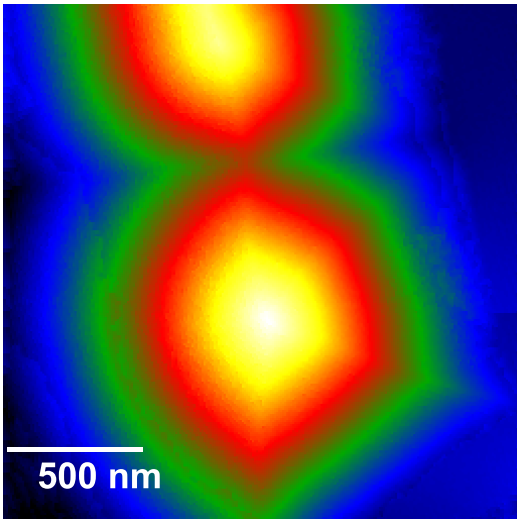

FIG. 4: Phase image (right) of nano-crystalline $Fe_{94}N_5Zr_1$.

The first term in Eq.(5) is in particular relevant to the examination of the cuboidal shape of nanostructured clusters[5]. The reconstructed phase from an electron hologram of a Mo cluster is shown in Fig. 3. The nearly constant phase in the projected object reconstructed from holograms acquired in several orientations close to $\langle 100 \rangle$ zone axis in order to minimize dynamical diffraction effects[6] excludes a cuboctahedral crystal habit. Figure 4 shows the reconstructed phase, using of the second term in Eq. (5), for nano-crystalline $Fe_{94}N_5Zr_1$.

¿From Eqs. (3-5) it is evident that finding the electrical potential and/or magnetic field of the sample that yields the experimentally observed set of amplitudes $A_o(\mathbf{r})$ and phases $\phi_o(\mathbf{r})$ requires the solution of a very difficult inverse problem. A more direct approach to answer this question is to consider various geometries of the sample, use a model for the electrical potential and magnetic field in the sample, and compute the amplitude and phase . This is the route presented in this paper.

II. THEORY

The calculation of the phase $\phi_o(\mathbf{r})$ and the amplitude $A_o(\mathbf{r})$ is simplified by making the following, standard assumptions[7]:

- The object acts as a phase object. This implies that we assume that the sample does not affect the amplitude $A_o(\mathbf{r})$.

- Effects of the interaction of the spin of the electron with the sample are ignored.

Both these assumptions are physically reasonable provided that the sample is sufficiently thin, which is usually the case in transmission electron microscopy. With these assumptions, the interaction of the electron wave and the sample is described by the Klein-Gordon equation[8]

$$\frac{1}{c^2}\left[E - e\Phi(\mathbf{r})\right]^2 \psi(\mathbf{r}) = \left(\left[-i\hbar\nabla - \frac{e}{c}\mathbf{A}(\mathbf{r})\right]^2 + m_0^2c^2\right)\psi(\mathbf{r}), \tag{6}$$

where $\Phi(\mathbf{r})$ is the scalar potential, $\mathbf{A}(\mathbf{r})$ is the vector potential, m_0 the rest mass of the electron and E the total relativistic energy of the electron.

The phase $\phi_o(\mathbf{r})$ can be computed by assuming a wave function of the form of Eq.(2) and applying the WKB approximation[8]. In the following treatment the reference beam $\psi_r(\mathbf{r})$ does not play a role. Therefore we can simplify the notation and write $\phi(\mathbf{r})$ for the phase shift of the object beam. Choosing the z-axis along the direction of the electron beam, the path of integration is also along the z-axis and the phase $\phi(x, y)$ is given by[7]

$$\begin{aligned}
\phi(x,y) &= \phi_e(x,y) + \phi_m(x,y), \\
\phi_e(x,y) &= \frac{\pi}{\lambda\tilde{E}}\int_{-\infty}^{\infty} V(x,y,z)dz, \\
\phi_m(x,y) &= -\frac{\pi}{\Phi_0}\int_{-\infty}^{\infty} A_z(x,y,z)dz,
\end{aligned} \tag{7}$$

where ϕ_e is the electric contribution to the phase, ϕ_m the magnetic contribution to the phase, $\Phi_0 = h/(2e) = 2.07 \times 10^3\,\mathrm{T\,nm^2}$ the flux quantum, and

$$\tilde{E} = \frac{E^2 - E_0^2}{2E}, \tag{8}$$

with E_0 the rest energy. Note that the phase $\phi(\mathbf{r})$ depends on the potentials $V(x, y, z)$ and $A_z(x, y, z)$, an example of the Aharonov-Bohm effect[9].

The key feature of electron holography is that a hologram contains a record of both the phase and the amplitude of the measurement beam, whereas traditional techniques record the amplitude only. Figure 1 shows the configuration for off-axis electron holography[7]. One part of the electron beam, the *object beam*, illuminates the sample is collected by a lens. The other part of the beam, the *reference beam*, propagates undisturbed to the same lens.

In order to proceed, we have to relate the two contributions in Eq.(7) to the properties of the sample. We assume that the electric potential $V(x, y, z)$ is dominated by the average, inner potential V_0. The electric phase shift ϕ_e then becomes

$$\phi_e(x,y) = \frac{\pi V_0}{\lambda\tilde{E}} l_z(x,y), \tag{9}$$

where $l_z(x, y)$ is the height of the object in the z-direction. In general, the vector potential $\mathbf{A}(\mathbf{r})$ for a magnetization $\mathbf{M}(\mathbf{r})$ is given by [11]

$$\mathbf{A}(\mathbf{r}) = \frac{\mu_0}{4\pi}\int_V \mathbf{M}(\mathbf{r}') \times \frac{\mathbf{r} - \mathbf{r}'}{|\mathbf{r} - \mathbf{r}'|^3}\mathrm{d}r', \tag{10}$$

where the integration extends over the volume V of the magnetized object. The most simple case is that of a magnetization $\mathbf{M}(\mathbf{r})$ that is constant throughout the sample:

$$\mathbf{M} = M_0(\cos\beta, \sin\beta, 0). \tag{11}$$

Here, we used the fact that $M_z(\mathbf{r})$ does not enter the expression of phase $\phi_m(\mathbf{r})$ and therefore, we can put it to zero without loss of generality. Substitution of Eq.(11) into Eq.(10) yields

$$\phi_m(x,y) = -\frac{\mu_0 M_0}{2\Phi_0}\int \mathrm{d}x' \int \mathrm{d}y' \frac{(y - y')\cos\beta - (x - x')\sin\beta}{(x - x')^2 + (y - y')^2} l_z(x', y'), \tag{12}$$

where the integration is over the volume of the object and $l_z(x', y')$ is the height of the object in the z-direction. Except for some simple geometries (see Appendix A), it is difficult to calculate Eq.(12) analytically and we have to resort to numerical methods to compute Eq.(12) (see Section III).

An alternative method to perform the integrals in Eq.(10) is to consider the Fourier transform of Eq.(10)[12–15]:

$$\mathbf{A}(\mathbf{k}) = \frac{\mu_0}{4\pi}\mathbf{M}(\mathbf{k}) \times \mathcal{F}\left(\frac{\mathbf{r}}{|\mathbf{r}|^3}\right) = -\frac{i\mu_0}{k^2}\mathbf{M}(\mathbf{k}) \times \mathbf{k}, \tag{13}$$

where k denotes the magnitude of $\mathbf{k}$. In the case of a constant magnetization inside the sample, we have

$$\mathbf{M}(\mathbf{r}) = M_0 \hat{m} D(\mathbf{r}), \tag{14}$$

where $\hat{m}$ is the direction of magnetization and $D(\mathbf{r})$ is the shape function, describing the geometry of the sample. Inserting Eq.(14) into equation Eq.(13) we get

$$\mathbf{A}(\mathbf{k}) = -\frac{i\mu_0 M_0}{k^2} D(\mathbf{k})(\hat{m} \times \mathbf{k}). \tag{15}$$

Substituting Eq.(15) into Eq.(7) and performing the z-integration in k space gives[14]

$$\phi_m(\mathbf{k}) = \frac{i\pi\mu_0 M_0}{\Phi_0} \frac{D(k_x, k_y, 0)}{k_x^2 + k_y^2} (\hat{m} \times \mathbf{k})\Big|_z . \tag{16}$$

In the Fourier space approach, the computation of the integral Eq.(12) has been replaced by a calculation of the Fourier transform of the function describing the geometrical shape of the sample and a Fourier transform of Eq.(16) to map the phase information to real space. Except for very simple cases, we have to resort to numerical methods to compute these Fourier transforms.

III. NUMERICAL METHODS

From the discussion of Section III, it is clear that, given the shape of the sample and within the approximations used to obtain the expressions for $\phi_e(\mathbf{r})$ and $\phi_m(\mathbf{r})$ (or, equivalently $\phi_m(\mathbf{k})$), the former is directly related to the shape whereas relating the latter to the shape requires the calculation of the integral of Eq.(12). In general, this calculation involves numerical work and in this section, we discuss two method to evaluate Eq.(12). In Appendix A, we collect some known and also present new analytical results for simple geometries. We use these examples to validate the numerical procedures. Because of its apparent simplicity and elegance, we first consider the Fourier space approach[12–15]. Then, we discuss a real-space method to compute the phase.

A. The Fast Fourier Transform

In general, the Fourier transforms of $D(\mathbf{r})$ and $\phi_m(\mathbf{r})$ can be computed efficiently by means of the Fast Fourier Transform (FFT) algorithm[16]. The calculation of the FFT of the shape function $D(\mathbf{r})$ does not present serious problems but performing the inverse FFT of $\phi_m(\mathbf{k})$ requires some attention. From Eq.(16), we see that $\phi_m(\mathbf{k}) \propto 1/k$ for $k \to 0$, behavior that is intrinsic as it is directly related to the slow decay ($\mathcal{O}(1/r)$) of $\phi_m(\mathbf{r})$ for large r. One possibility to alleviate this problem is to multiply the real-space expression by a (Gaussian) window to such that real-space function vanishes at the edges of the real-space domain of interest. In Fourier space, this amount to the computation of the convolution of $\phi_m(\mathbf{k})$ with the Fourier transform of the window. Obviously, this is a computationally expensive procedure. Alternatively, we can eliminate the numerical problem of having to divide by zero by 1) shifting the k-space grid by one half of the grid spacing in each of the two directions or 2) by adding a small number ϵ to numerator in Eq.(16), that is we replace $1/(k_x^2 + k_y^2)$ by $1/(k_x^2 + k_y^2 + \epsilon^2)$. In the latter case, we have to study the convergence of the phase image as a function of ϵ. Furthermore, as $\phi_m(\mathbf{k})$ decays slowly as $k \to \infty$, we multiply $\phi_m(\mathbf{k})$ by a window that vanishes rapidly as $k \to \infty$. In our numerical work, we use a Gaussian window. Extensive tests (results not shown) on exactly solvable geometries (see Appendix A) demonstrate that both methods give results of similar quality. Our numerical experiments indicate that the first method yields the smallest the difference between exact and FFT results.

In Fig. 5(a), we show the magnetic contribution $\phi_m(\mathbf{r})$ for a slab (tilt angle $\theta = 0°$). In all our examples we use $\mu_0 M_0 = 1.6\,\mathrm{T}$ as in ref 13. To perform the FFTs, we use $N = 4096$ points for each of the two directions and a mesh in k-space corresponding to a real-space mesh size of 1 nm. Figure 5(b) shows the difference between the exact, analytical solution and the $\phi_m(\mathbf{r})$, as obtained by the Fourier space approach. The numerical method yields satifisfactory results if we limit ourselves to the region of interest, indicated by the translucent square.

A disadvantage of the Fourier space approach is that it rapidly becomes computationally very expensive if we have to increase the accuracy or have to consider samples of increasing real-space size. In both cases, we have to increasing the number of mesh points N^2 in k-space, whereas in the end, we are only interested in $\phi_m(\mathbf{r})$ for a relatively small region in real space. Thus, for these applications, the Fourier approach looses efficiency.

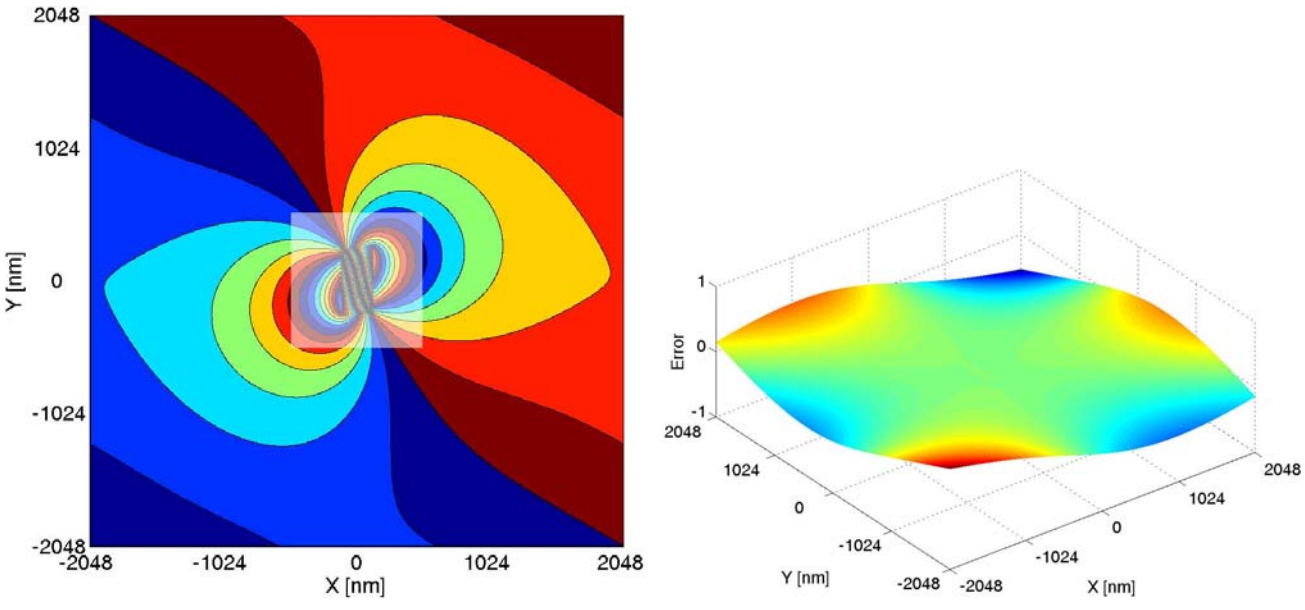

FIG. 5: (a) The magnetic phase shift ϕ_m (amplified 2 times) of a slab with $L_x = 256\,\text{nm}$, $L_y = 512\,\text{nm}$, $L_z = 32\,\text{nm}$, $\theta = 0^\circ$ and $\beta = 300^\circ$. The Fast Fourier transforms were carried out using $N = 4096$ points for each of the two directions. The translucent area indicates where the error (relative to the exact result) is below one percent. (b) The difference of the numerical solution of ϕ_m and the exact analytical result (see Appendix A).

B. Real-space approach

As an alternative to the FFT-based approach, we explore the possibility to compute Eq.(12) directly, in real space, using the most simple numerical integration scheme, the trapezium rule. Obviously, because we use the real-space expression Eq.(12), this approach has no problems dealing with the slow long-distance decay of the vector potential. However, from Eq.(12), we see that the price we pay for circumventing this problem is that we have to find a way to handle the singular integrand in Eq.(12). The problems originating from the singular nature of the integrand in Eq.(12) can be solved by careful examination of the various cases:

1. Consider points (x, y) that are not at the boundary of the sample. If l_z does not depend on (x, y), the integrand of Eq.(12) is anti-symmetric around the point $(x', y') = (x, y)$. Changing variables $x'' = x - x'$ and $y'' = y - y'$, Eq.(12) becomes

$$\phi_m(x, y) = -\frac{\mu_0 M_0}{2\Phi_0} \int \mathrm{d}x'' \int \mathrm{d}y'' \frac{y'' \cos\beta - x'' \sin\beta}{x''^2 + y''^2}. \tag{17}$$

   The anti-symmetry implies that contributions of points that are placed symmetrically around $(x'', y'') = (0, 0)$ cancel each other *exactly*. Thus, if the numerical integration scheme uses a grid in which the points are chosen to lay symmetrically around $(x'', y'') = (0, 0)$, the contribution of the singular point vanishes.

2. If there is an integrable singularity at $(x', y') = (x, y)$, we have two options. The first is to move the grid such that (x, y) falls between two grid points. However, in general this will lead to a loss of accuracy. The second option is to put $(x', y') = (x, y)$ on a grid point and exclude the point (x, y) in the numerical integration procedure, as illustrated in Fig.6. The integration over the excluded area has to be done analytically. If l_z does not depend on (x, y), we already know that this contribution to the integral vanishes. In general, if l_z changes smoothly with (x, y) (on the scale of the grid), assuming that l_z does not depend on (x, y) yields a good approximation for the (zero) contribution to the integral.

3. A special case occurs if (x, y) is on the boundary of the object. Then (part of) the symmetry will be broken. Here we also have two options. Either we calculate the integral analytically or we simply avoid evaluations on the boundary of the object by an appropriate choice of the grid. For practical purposes, we choose the second options.

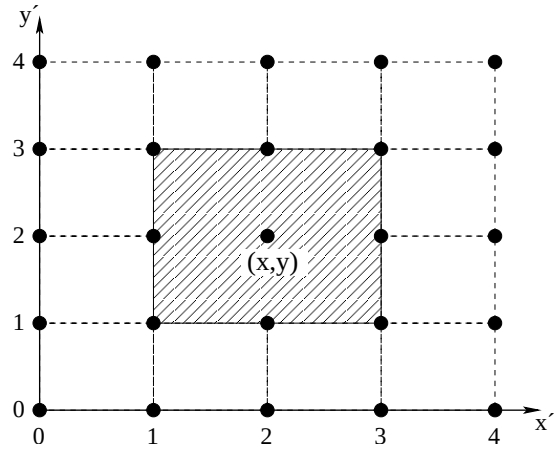

FIG. 6: The contribution of the singularity of the integrand in Eq.(12) at $(x', y') = (x, y)$ is evaluated by choosing the grid such that (x, y) lies on the grid and by excluding the point (x, y) from the integration procedure.

We have implemented this method, employing the most simple numerical integration technique, namely the trapezium rule[16]:

$$\int_a^b f(x)\mathrm{d}x = \Delta[f_1/2 + f_2 + \ldots + f_{N-1} + f_N/2] + \mathcal{O}(N^{-2}), \tag{18}$$

applied to the two coordinates x and y, with different mesh size Δ if necessary. The combination of simplicity and flexibility to manipulate the grid make it an attractive integration method.

In Fig.7(a) we show results for the example of Fig.5, as obtained by the real-space method. For this calculation, we employ a grid of 256×256 points. This calculation must be repeated for every point in the phase map. Therefore the total number of computations in much greater then in the FFT calculation.

It is clear from the error (relative to the exact solution) depicted in Fig. 7(b), that there is excellent agreement with the exact result for the whole range of (x, y)-values.

IV. APPLICATIONS

In this section, we apply the numerical procedure outlined above to two nontrivial examples. In the first example, we consider a slab with surface roughness and compute the phase map for two different models of the roughness. Then, we explore the effect of a presence of domain walls on the phase map.

A. Slab with a rough surface

Consider a slab of dimensions $L_x \times L_y \times L_z$, with a magnetization given by Eq.(11). The surface roughness is conveniently modeled by specifying the height function $h(\mathbf{k})$, such that the volume V of the slab is given by

$$V = \int_0^{L_x} dx \int_0^{L_y} dy \int_0^{L_z + h(x,y)} dz, \tag{19}$$

and all integrations over the volume V are to be performed in a similar manner. In general, the correlation function of the surface heights is given by

$$C(\mathbf{r}) = \frac{1}{A}\int_A < h(\mathbf{r}' + \mathbf{r})h(\mathbf{r}) > \mathbf{dr}, \tag{20}$$

where A is the area of the projection of the surface onto the (x, y)-plane. According to the Wiener-Khinchin theorem,

$$< |h(\mathbf{k})|^2 >= \frac{A}{64\pi^6}\int C(\mathbf{r})e^{-i\mathbf{k}\cdot\mathbf{r}}\mathbf{dr}, \tag{21}$$

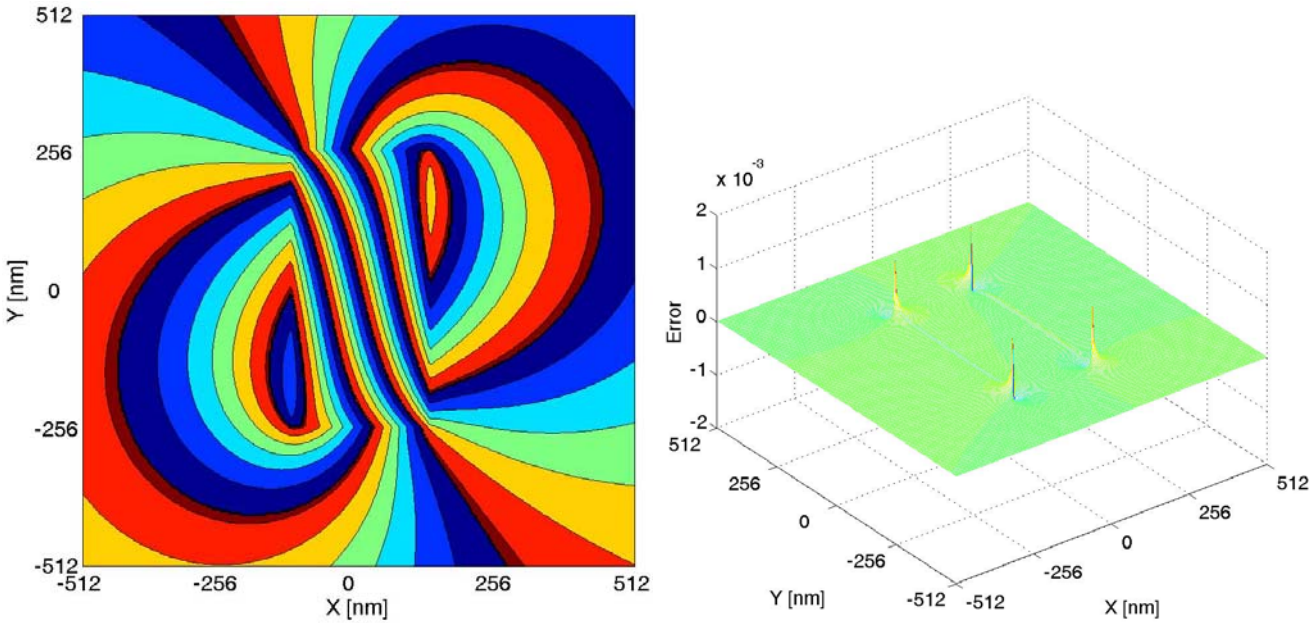

(a) (b)

FIG. 7: (a) The magnetic phase shift ϕ_m (amplified 2 times) of a slab with $L_x = 256\,\text{nm}$, $L_y = 512\,\text{nm}$, $L_z = 32\,\text{nm}$, $\theta = 0^\circ$ and $\beta = 300^\circ$, as obtained by the real-space method using a grid of 256×256 points; (b) The difference of the numerical solution of ϕ_m and the exact analytical result (see Appendix A). For $|x| > 512$ nm or $|y| > 512$ nm, this difference is too small to be seen on the scale of 10^{-3} (results not shown).

we can characterize the roughness through the Fourier coefficients. For an isotropic, self-affine surface, each $h(\mathbf{k})$ is a Gaussian random variable with zero average and variance $< |h(k)|^2 >$ given by[17,18]

$$< |h(k)|^2 >= \frac{A}{32\pi^5} \frac{\alpha \xi^2 w^2}{(1+\xi^2 k^2)^{1+\alpha}}, \tag{22}$$

where w is the amplitude of the fluctuations, ξ the lateral correlation length and α the roughness exponent, with $0 \leq \alpha \leq 1$. Adopting the model of Eq.(22) for the surface roughness, the surface ($h(\mathbf{r})$) itself is readily constructed by generating Gaussian random numbers with variance Eq.(22), followed by a Fourier transformation.

Figure 8 depicts examples of such surfaces for $\alpha = 1/2$ and $\alpha = 1$. From Fig.9, it is clear that $\phi_e(\mathbf{r})$ changes significantly with the roughness exponent α. However, the effect of the surface roughness on $\phi_m(\mathbf{r})$ is small (results not shown). In Fig.10, we show the total phase $\phi(\mathbf{r}) = \phi_e(\mathbf{r}) + \phi_m(\mathbf{r})$. The fluctuations on the lines of constant phase are mainly due to $\phi_e(\mathbf{r})$.

B. Slabs with a domain walls

We consider a slab of magnetic material of width L_x, length L_y and height L_z, containing two magnetic domains, as shown in Fig. 11. The two domains are separated by a region containing a domain wall. In this region, the direction of the magnetization rotates in the x=z plane from $(M_0, 0, 0)$ to $(-M_0, 0, 0)$. The expression for the magnetization describing the domain wall is given by[19]

$$\mathbf{M}(y) \;=\; M_0(\cos\theta, 0, \sin\theta), \tag{23}$$

where

$$\theta \;=\; 2\arctan e^{\lambda y}, \tag{24}$$

The parameter λ determines the width of the domain wall.

In Fig. 12, we show our numerical results for two slabs containing a single domain wall, centered at $y = 0$. The main structure in these phase images is replicated if the slab contains more than one domain wall, as illustrated in Fig. 13.

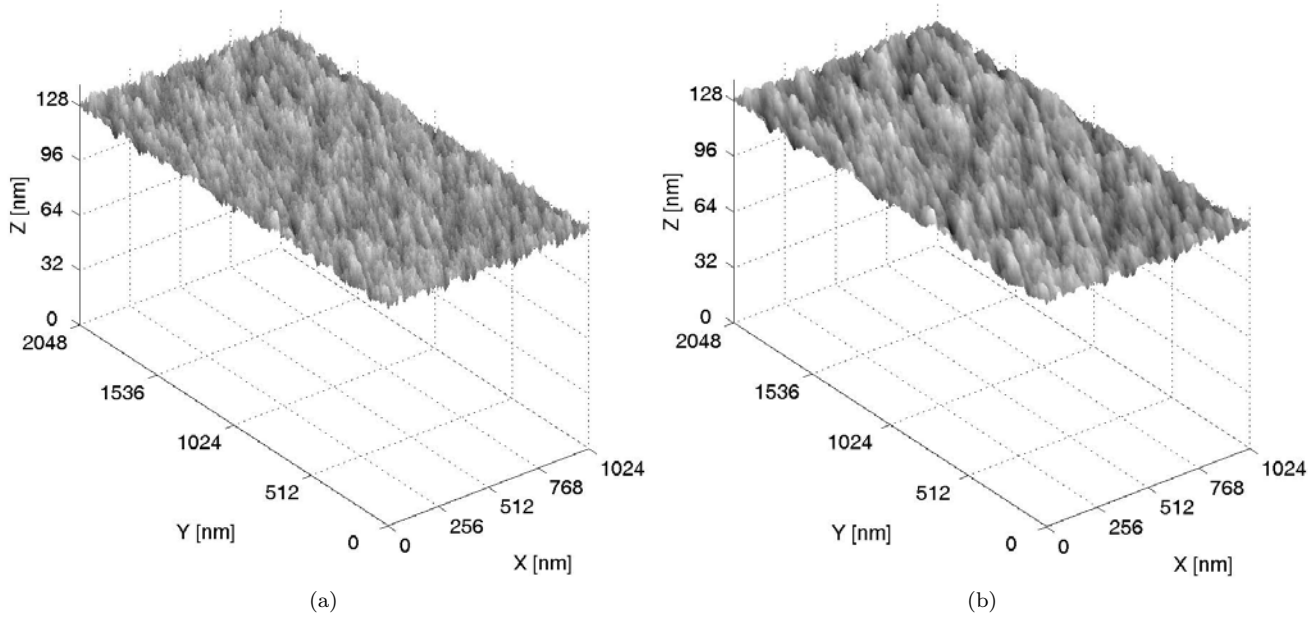

FIG. 8: Surface of a rough slab of dimensions 1024 nm × 2048 nm × 128 nm. The surface roughness is generated using Eq. (22) with $w = 0.5$ nm, $\xi = 32$ nm. (a) $\alpha = 1/2$; (b) $\alpha = 1$.

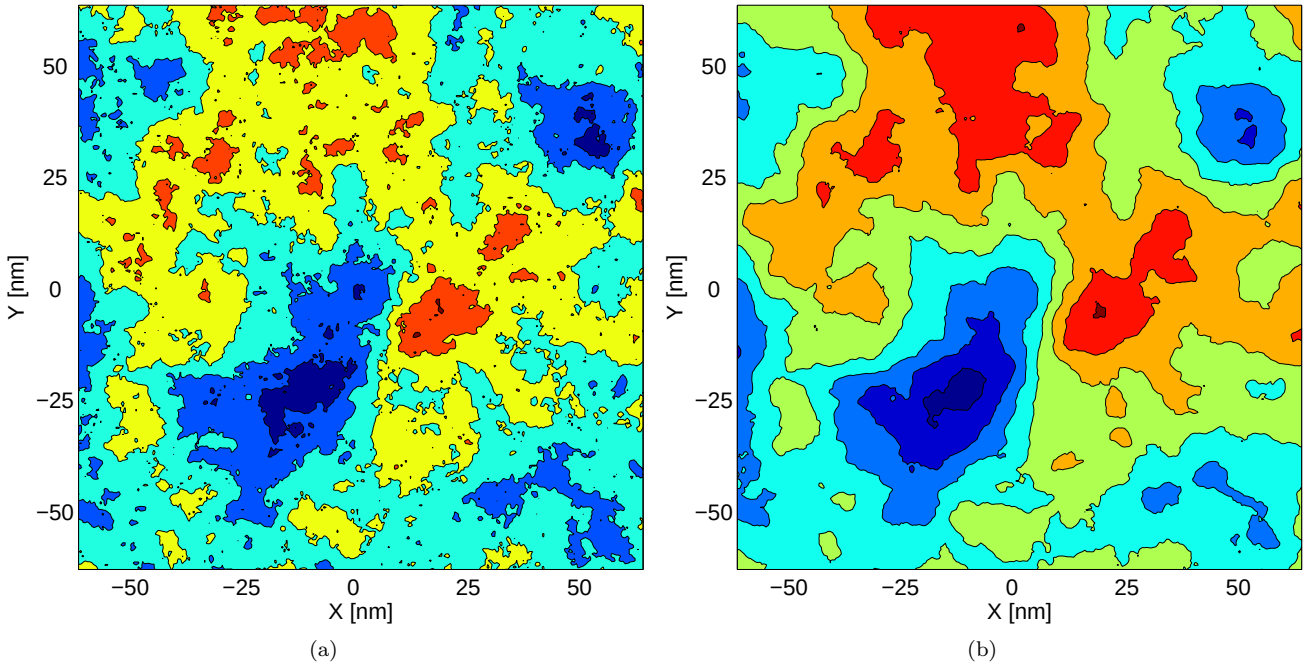

FIG. 9: Electrical phase shift ϕ_e for the slabs depicted in Fig.8.

V. SUMMARY

We have analysed two different computational methods to calculate the phase images of nanoscale particles, as observed by electron holography. In general, both the Fourier transform approach[12] and the real-space method presented in this paper are found to yield accurate results for the phase images of simple geometries for which analytical results are available. For these geometries, the real-space technique is computationally less efficient than the Fourier-space method, but the latter looses its advantages if the domain (in real-space) of interest is a small fraction from the space that is required to perform accurate Fourier transforms. The real-space technique is more

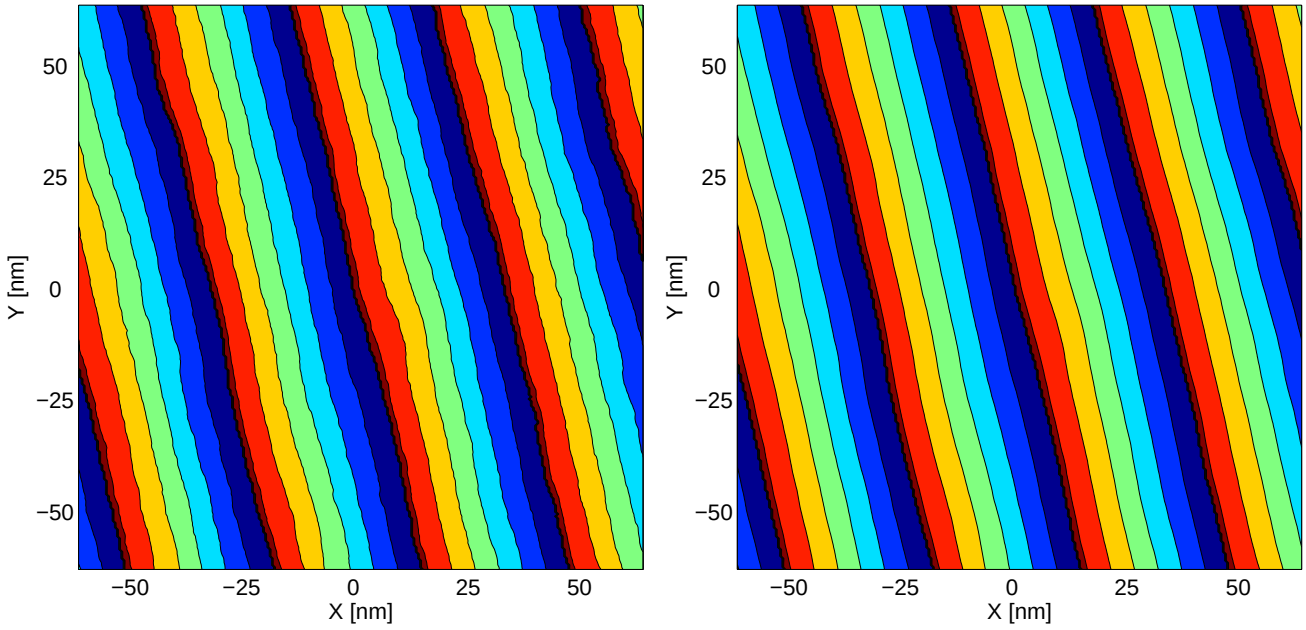

FIG. 10: Total phase (without amplification))$\phi = \phi_m + \phi_e$ for the slabs depicted in Fig.8.

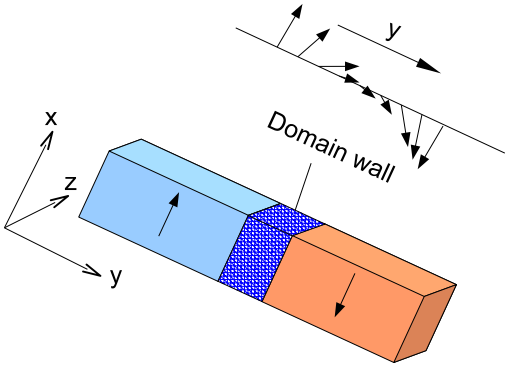

FIG. 11: Schematic diagram of a slab containing two magnetic domains, separated by domain wall. The magnetization $\mathbf{M}$ rotates in the $\hat{x} - \hat{y}$ plane from $(M_0, 0, 0)$ to $-(M_0, 0, 0)$. We optionally tilt the slab by rotating it around the $\hat{x}$ axis.

flexible in this respect. We illustrate this by employing the real-space approach to compute the electron holography phase images of slabs with surface roughness and slabs containing magnetic domain walls. Although this paper focused on magnetic particles, with minor modifications the computational techniques can also be applied to compute the electron holography phase images of ferroelectric particles .

APPENDIX A: ANALYTICAL SOLUTIONS TO SIMPLE GEOMETRIES

In this appendix, we give some known and new analytical expressions of the phase shift for various simple geometries. These analytical solutions are extremely valuable to assess the accuracy of numerical methods.

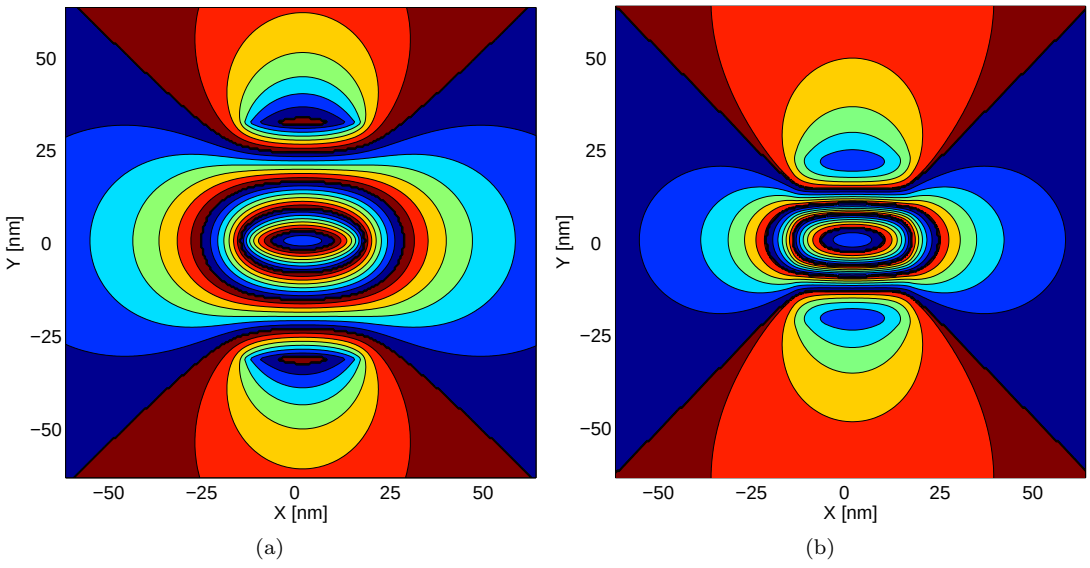

FIG. 12: (a) Magnetic phase shift ϕ_m (amplified 32 times) of a slab of dimensions $L_x = 32\,\text{nm}$, $L_y = 64\,\text{nm}$, $L_z = 16\,\text{nm}$ containing a domain wall centered at $y = 0$. The magnetization inside the domain wall is given by Eq. (24) with $\lambda = 1/2$; (b) Same system as in (a) except that the slab is tilted by 60° about the in the $\hat{x}$ axis. The large tilt angle was chosen to make the effect of the tilt clearly visible.

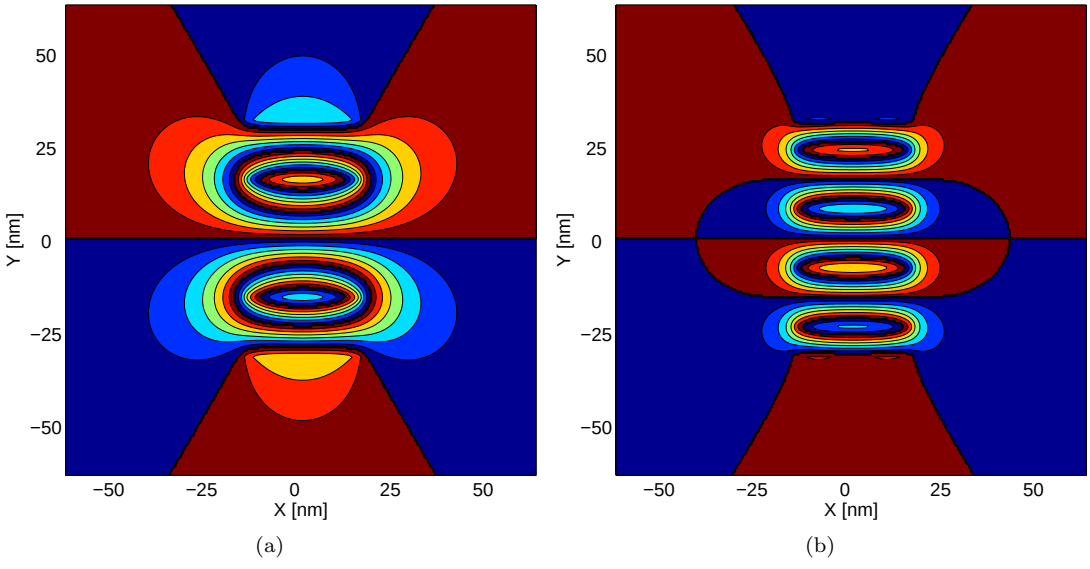

FIG. 13: (a) Magnetic phase shift ϕ_m of a slab (amplified 32 times) $L_x = 32\,\text{nm}$, $L_y = 64\,\text{nm}$, $L_z = 16\,\text{nm}$ containing two domain walls located at $y = \pm 16\,\text{nm}$. The magnetization inside the domain wall is given by Eq. (24) with $\lambda = 1$; (b) Same system as in (a) except that are four domain walls located at $y = \pm 8\,\text{nm}$ and at $y = \pm 24\,\text{nm}$.

1. Magnetized slab

The first case we consider is that of the uniformly magnetized slab. Let the magnetized slab have width L_x, length L_y and height L_z and a uniform magnetization given by Eq. (11). From Eq. (12) we see that the magnetic phase shift for the slab is given by

$$\phi_m(x,y) = -\frac{\mu_0 M_0 L_z}{2\Phi_0}\int_{-L_x/2}^{L_x/2} \mathrm{d}x' \int_{-L_y/2}^{L_y/2} \mathrm{d}y' \frac{(y-y')\cos\beta - (x-x')\sin\beta}{(x-x')^2 + (y-y')^2}, \tag{A1}$$

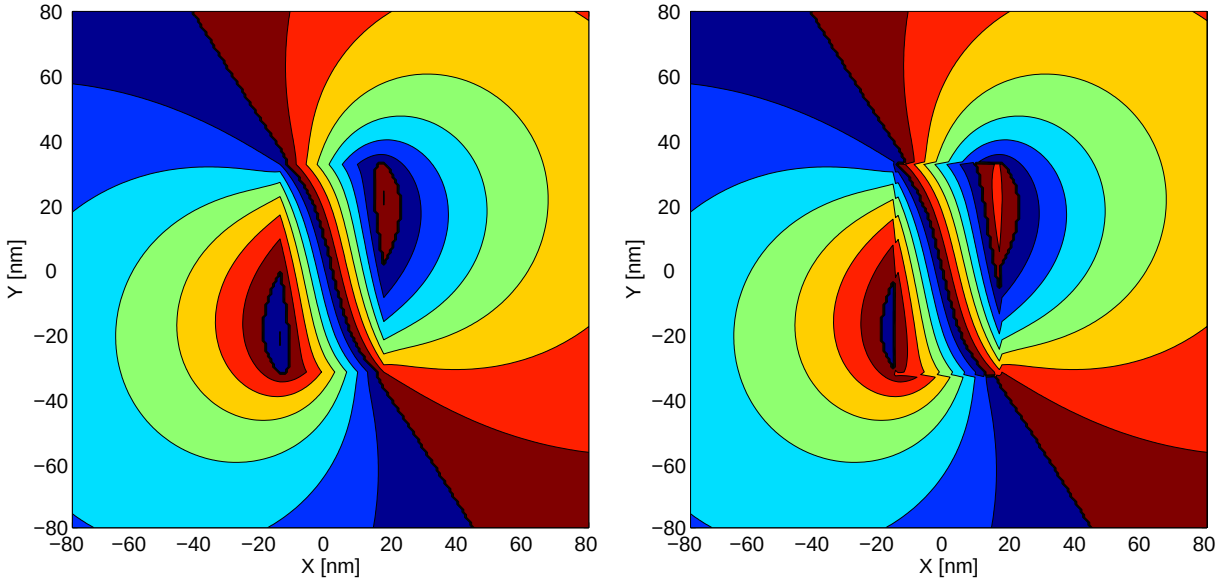

(a) (b)

FIG. 14: (a) Magnetic phase shift ϕ_m (amplified 16 times) for a slab of dimensions $L_x = 32\,\text{nm}$, $L_y = 64\,\text{nm}$, and $L_z = 16\,\text{nm}$. We use the following parameters: Magnetization direction $\beta = 300°$, inner potential $V_0 = 1\,\text{V}$, and 200 kV electrons; (b) Total phase shift $\phi = \phi_e + \phi_m$, amplified 16 times.

which can be evaluated in closed form by using the identity (see e.g. equation 2.733.1 from Ref. 22)

$$F_0(x,y) = \int \ln(x^2+y^2)\mathrm{d}x = x\ln(x^2+y^2) - 2x + 2y\arctan(x/y). \tag{A2}$$

We obtain

$$\begin{aligned}\phi_m(\mathbf{r}) = &-\frac{\mu_0 M_0 L_z}{4\Phi_0}\left[F_0(x-L_x/2, y-L_y/2) - F_0(x+L_x/2, y-L_y/2) - \right.\\ &\left. F_0(x-L_x/2, y+L_y/2) + F_0(x+L_x/2, y+L_y/2)\right]\cos\beta + \\ &\frac{\mu_0 M_0 L_z}{4\Phi_0}\left[F_0(y-L_y/2, x-L_x/2) - F_0(y+L_y/2, x-L_x/2) - \right.\\ &\left. F_0(y-L_y/2, x+L_x/2) + F_0(y+L_y/2, x+L_x/2)\right]\sin\beta.\end{aligned} \tag{A3}$$

The electric contribution to the phase is given by Eq. (9). In this case, the only effect of the electric contribution is to add a constant offset to the total phase shift inside the slab. In Fig. 14 we show an example of the phase map of the total phase.

2. Magnetized cylinder

Consider a magnetized cylinder of radius a and length l with a uniform magnetization given by Eq. (11). The phase shift is most easily calculated in Fourier space. Switching to cylindrical coordinates, we have

$$\begin{aligned} x &= r\cos\psi, \quad & y &= r\sin\psi, \quad & z &= z, \\ k_x &= k_\perp\cos\phi, \quad & k_y &= k_\perp\sin\phi, \quad & k_z &= k_z. \end{aligned} \tag{A4}$$

In cylindrical coordinates, the Fourier transform reads

$$F(\mathbf{k}) = \int f(\mathbf{r}) e^{-i\mathbf{k}\cdot\mathbf{r}}\mathrm{d}^3\mathbf{r} = \int f(\mathbf{r}) e^{-ik_z z} e^{-ik_\perp r\cos(\phi-\psi)} r\mathrm{d}r\mathrm{d}\psi\mathrm{d}z. \tag{A5}$$

Taking the Fourier transform of the shape function immediately gives the phase shift [14] in Fourier space:

$$\phi(\mathbf{k}) = i\frac{2\pi^2 B_0 a l}{\Phi_0}\frac{k_y\cos\beta - k_x\sin\beta}{k_\perp^3} J_1(k_\perp a), \tag{A6}$$

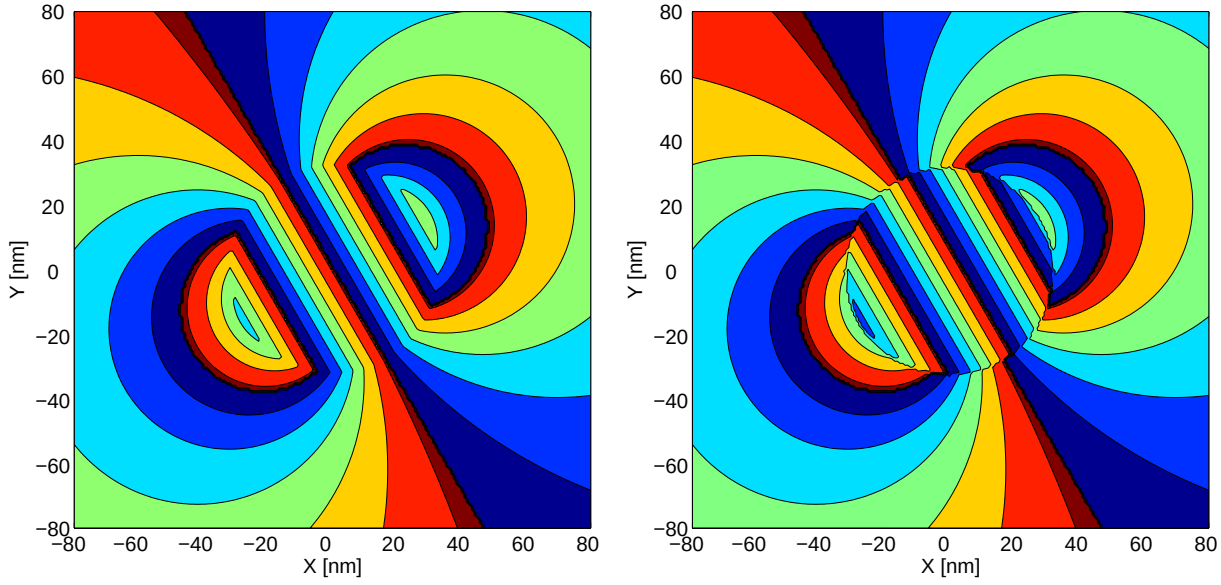

(a) (b)

FIG. 15: (a) Magnetic phase shift ϕ_m (amplified 16 times) for a cylinder of radius $a = 32\,\text{nm}$ and length $l = 16\,\text{nm}$. We use the following parameters: Magnetization direction $\beta = 300°$, inner potential $V_0 = 1\,\text{V}$, and 200 kV electrons; (b) Total phase shift $\phi = \phi_e + \phi_m$, amplified 16 times.

with $J_1(x)$ a Bessel function of the first kind. The inverse Fourier transform of Eq. (A6) is

$$\phi(x,y) = \frac{ialB_0}{\Phi_0}\int_0^{\pi}\int_0^{\infty} e^{ik_\perp r\cos\theta}\frac{\cos\theta\sin\psi\cos\beta - \cos\theta\cos\psi\sin\beta}{k_\perp}J_1(k_\perp a)\mathrm{d}k_\perp\mathrm{d}\theta. \tag{A7}$$

Performing the θ integration gives

$$\phi(x,y) = -\frac{al\pi B_0}{\Phi_0}\int_0^{\infty}\frac{\sin\psi\cos\beta - \cos\psi\sin\beta}{k_\perp}J_1(k_\perp r)J_1(k_\perp a)\mathrm{d}k_\perp. \tag{A8}$$

Performing the final integration in Eq. (A8) (see e.g. chapter 11 of Ref. 23) gives the final result

$$\phi(x,y) = \begin{cases} -\pi la^2B_0(y\cos\beta - x\sin\beta)/(2\Phi_0 r^2) & (r > a) \\ -\pi lB_0(y\cos\beta - x\sin\beta)/(2\Phi_0) & (r < a) \end{cases}, \tag{A9}$$

In Fig. 15 we show an example of a phase map. As in the case of the rectangular slab, the effect of electric potential is to adds a constant offset to the total phase inside the object.

3. Magnetized sphere

Consider a magnetized sphere of radius a with a uniform magnetization given by Eq. (11). The magnetic phase shift an electron passing through the $\hat{z}$ direction gets is given by[20]

$$\phi_m(x,y) = \frac{2\pi B_0a^3(y\cos\beta - x\sin\beta)}{3\Phi_0r^2}\times\begin{cases} 1-[1-(r^2/a^2)]^{3/2} & r < a \\ 1 & r \geq a \end{cases}, \tag{A10}$$

with $r = \sqrt{x^2+y^2}$. In Fig. 16, we show an example of an image of the total phase for a sphere of radius $a = 32\,\text{nm}$.

4. Tilted slab

It is common in electron holography experiments to tilt the sample, relative to the direction of the electron beam. Thus, it is of interest to have a closed form expression for the phase for at least one simple geometry that is tilted in

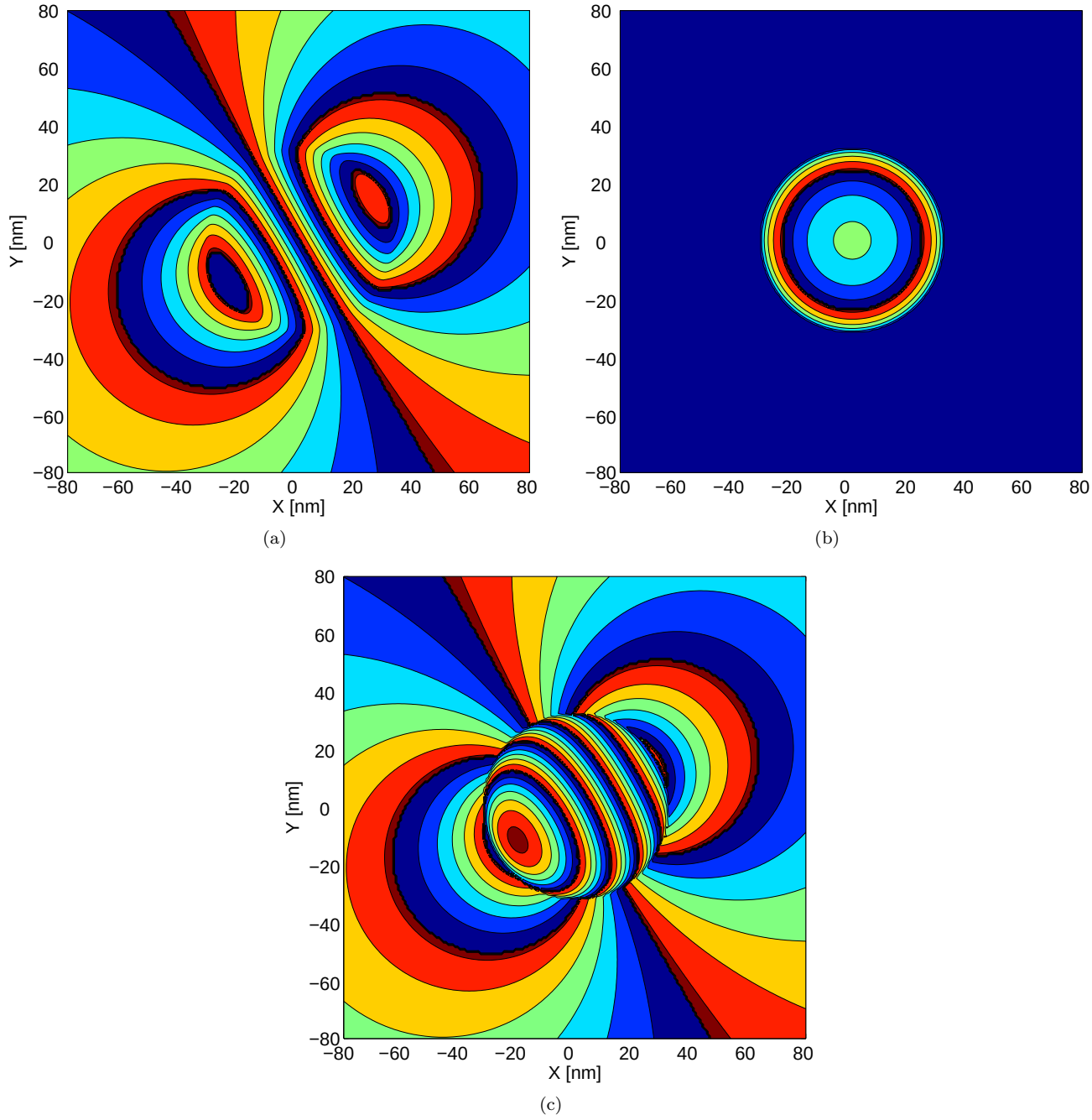

FIG. 16: (a) Magnetic phase shift ϕ_m (amplified 8 times) for a sphere of radius $a = 32\,\text{nm}$. The model parameters are: Magnetization direction $\beta = 300°$, inner potential $V_0 = 1\,\text{V}$, and 200 kV electrons; (b) The electric phase shift ϕ_e, amplified 8 times; (c) Total phase shift $\phi = \phi_e + \phi_m$, amplified 8 times.

the same manner. We consider the rectangular, magnetized slab, tilted over an angle θ in the (y, z) plane such that

$$\mathbf{M} = M_0(\cos\beta, \sin\beta\cos\theta, \sin\beta\sin\theta). \tag{A11}$$

A schematic picture of this situation is shown in Fig. 17. The magnetic contribution to the phase, accumulated by an electron traveling along the z-direction, is given by

$$\phi_m(\mathbf{r}) = -\frac{\mu_0 M_0}{2\Phi_0}\int_V \mathrm{d}^3\mathbf{r}'\,\frac{(y-y')\cos\beta - (x-x')\sin\beta\cos\theta}{(x-x')^2+(y-y')^2}. \tag{A12}$$

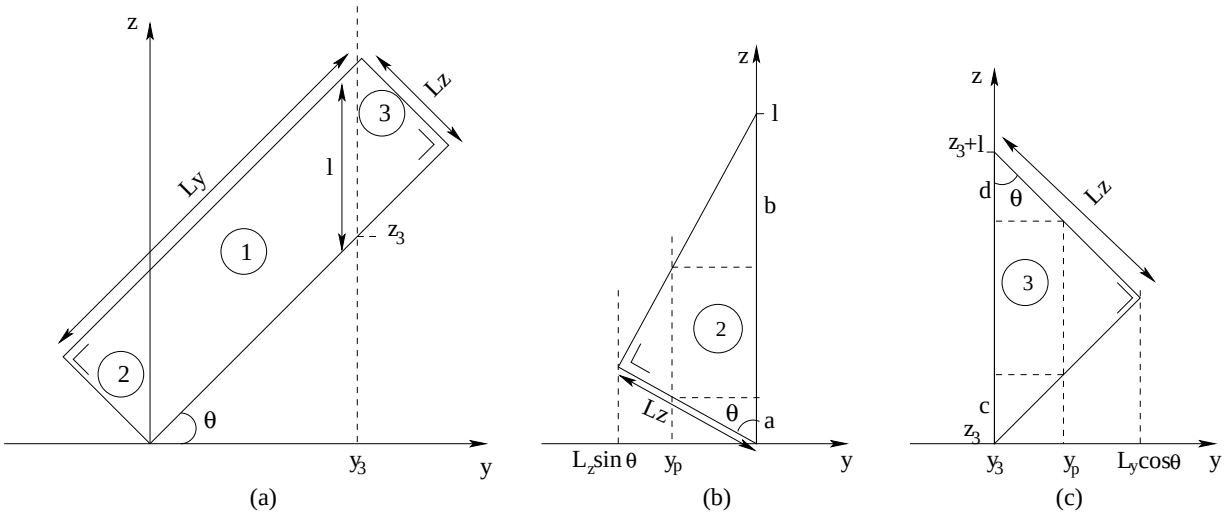

FIG. 17: a) Slab of dimensions $L_x \times L_y \times L_z$ tilted over an angle of θ degrees. For the evaluation of the total phase shift we divide the tilted slab into three regions as indicated by the numbered circles; b) Region 2 of the tilted slab. Here y_p is the point that we are currently evaluating; c) Region 3 of the magnetized slab. Here y_p is the point that we are currently evaluating.

To carry out the integral over the volume, we split the slab into three regions, as shown in Fig. 17. We consider each integral separately.

Region one: The calculation of the phase is almost identical to the untilted case. We find

$$\begin{aligned}\phi_m(\mathbf{r}) = -\frac{\mu_0 M_0 L_z}{4\Phi_0 \cos\theta}\,[F_0(x-L_x, y-y_3) - F_0(x+L_x, y-y_3) - \\ F_0(x-L_x, y+y_3) + F_0(x+L_x, y+y_3)]\cos\beta + \\ \frac{\mu_0 M_0 L_z}{4\Phi_0}\,[F_0(y-y_3, x-L_x) - F_0(y+y_3, x-L_x) - \\ F_0(y-y_3, x+L_x) + F_0(y+y_3, x+L_x)]\sin\beta,\end{aligned} \tag{A13}$$

where F_0 is given by Eq. (A2).

Region two: Substituting the integration boundaries into Eq. (A12) and performing the z' integration yields

$$\phi_m(x,y) = -\frac{\mu_0 M_0}{2\Phi_0}\int_x^{x-L_x} \mathrm{d}x'' \int_{y+L_z\sin\theta}^{y} \mathrm{d}y'' \;\frac{y''\cos\beta - x''\sin\beta\cos\theta}{y''^2 + x''^2}\left(\frac{L_z}{\cos\theta} + \frac{2(y-y'')}{\sin 2\theta}\right), \tag{A14}$$

where $x'' = (x - x')$ and $y'' = (y - y')$. Except for the last term $y''/\sin 2\theta$, Eq. (A14) is very similar to the calculation we did for region one. Therefore, we split equation(A14) in two parts $f(\mathbf{r})$ and $g(\mathbf{r})$ such that

$$\phi_m(\mathbf{r}) = -\frac{\mu_0 M_0}{2\Phi_0}(f(\mathbf{r}) - g(\mathbf{r})), \tag{A15}$$

and using the result for region one we find that

$$\begin{aligned}f(\mathbf{r}) = &\frac{y + L_z\sin\theta}{\sin 2\theta}\,\{[F_0(x-L_x, y) - F_0(x-L_x, y+L_z\sin\theta) - F_0(x,y) + F_0(x, y+L_z\sin\theta)]\cos\beta - \\ &[F_0(y, x-L_x) - F_0(y+Lz\sin\theta, x-L_x) - F_0(y,x) + F_0(y+Lz\sin\theta, x)]\cos\theta\sin\beta\}\end{aligned} \tag{A16}$$

where $F_0(x,y)$ is defined by Eq. (A2). The second integral $g(\mathbf{r}$ is straightforwardly evaluated and reads

$$\begin{aligned}g(\mathbf{r}) &= \frac{2}{\sin 2\theta}\int dx'' \int dy'' \quad \frac{y''\cos\beta - x''\sin\beta\cos\theta}{y''^2 + x''^2} y'' \\ &= F_1(x-L_x, y) - F_1(x-L_x, y+L_z\sin\theta) - F_1(x,y) + F_1(x, y+L_z\sin\theta)\ ,\end{aligned} \tag{A17}$$

where $F_1(x,y)$ is given by

$$F_1(x,y) = \frac{\cos\beta}{\sin 2\theta}\left(xy + y^2\arctan(x/y) - x^2\arctan(y/x)\right) - \frac{\cos\theta\sin\beta}{2\sin 2\theta}\left(-x^2 + \left(x^2+y^2\right)\ln\left(x^2+y^2\right)\right). \tag{A18}$$

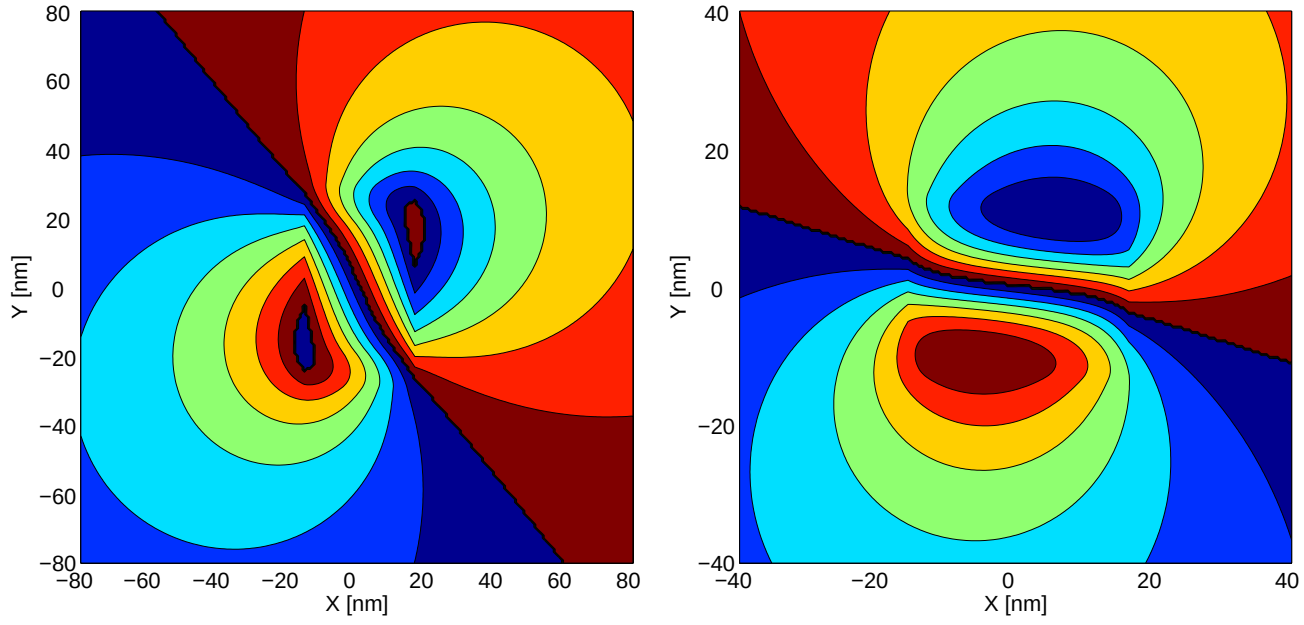

(a) (b)

FIG. 18: Magnetic contribution ϕ_m to the phase ϕ (amplified 16 times) for a slab of dimensions $L_x = 32\,\text{nm}$, $L_y = 64\,\text{nm}$, and $L_z = 16\,\text{nm}$, and magnetization direction $\beta = 300^\circ$: (a) $\theta = 40^\circ$; (b) $\theta = 80^\circ$.

Region three: The calculation for region three is identical to that of region two, except that the integration boundaries are different, as is clear from Fig. 17c. The magnetic contribution to the phase shift is given by

$$\phi_m(\mathbf{r}) = -\frac{\mu_0 M_0}{2\Phi_0}\int_0^{L_x} dx' \int_{y_3}^{L_y\cos\theta} dy' \quad \frac{(y-y')\cos\beta - (x-x')\sin\beta\cos\theta}{(x-x')^2+(y-y')^2}\left(\frac{L_z}{\cos\theta} - \frac{2(y'-y_3)}{\sin 2\theta}\right) \tag{A19}$$

and as before, we split the integral into two parts such that

$$\phi_m(\mathbf{r}) = -\frac{\mu_0 M_0}{2\Phi_0}(\hat{f}(\mathbf{r}) + g(\mathbf{r})), \tag{A20}$$

where $g(\mathbf{r})$ is given by Eq.(A17) and $\hat{f}(\mathbf{r})$ given by

$$\begin{aligned}\hat{f}(\mathbf{r}) = \frac{L_z\sin\theta + y - y_3}{\sin 2\theta}\{&[F_0(x-L_x, y-L_y\cos\theta) - F_0(x-L_x, y-y_3) \; -F_0(x, y-L_y\cos\theta) + F_0(x, y-y_3)]\cos\beta \\ &- [F_0(y-L_y\cos\theta, x-L_x) - F_0(y-y_3, x-L_x) \\ &- \; F_0(y-L_y\cos\theta, x) + F_0(y-y_3, x)]\cos\theta\sin\beta\}\,.\end{aligned} \tag{A21}$$

Putting all the pieces together, we can compute the total phase for an arbitrary inclinations θ. In Figs. 18(a) and 18(b) we plot the magnetic contribution to the phase, for inclination of 40° and 80°, respectively. In Figs.19(a) and (b) we plot the corresponding electric contribution phase for the same inclinations. In regions one and three, the electric part ϕ_e changes rapidly as a function of y and gives a large contribution to the structure in total phase. The large tilt angles were chosen to make the effect of the tilt clearly visible.

---

* Electronic address: k.keimpema@rug.nl
† Electronic address: h.a.de.raedt@rug.nl
‡ Electronic address: J.Th.M.De.Hosson@rug.nl

[1] D. Gabor, Proc. Roy. Soc. London **A197**, 454 (1949).
[2] A. Tonomura, *Electron Holography*, Springer Series in Optical Sciences 164, Springer, Berlin (1999)

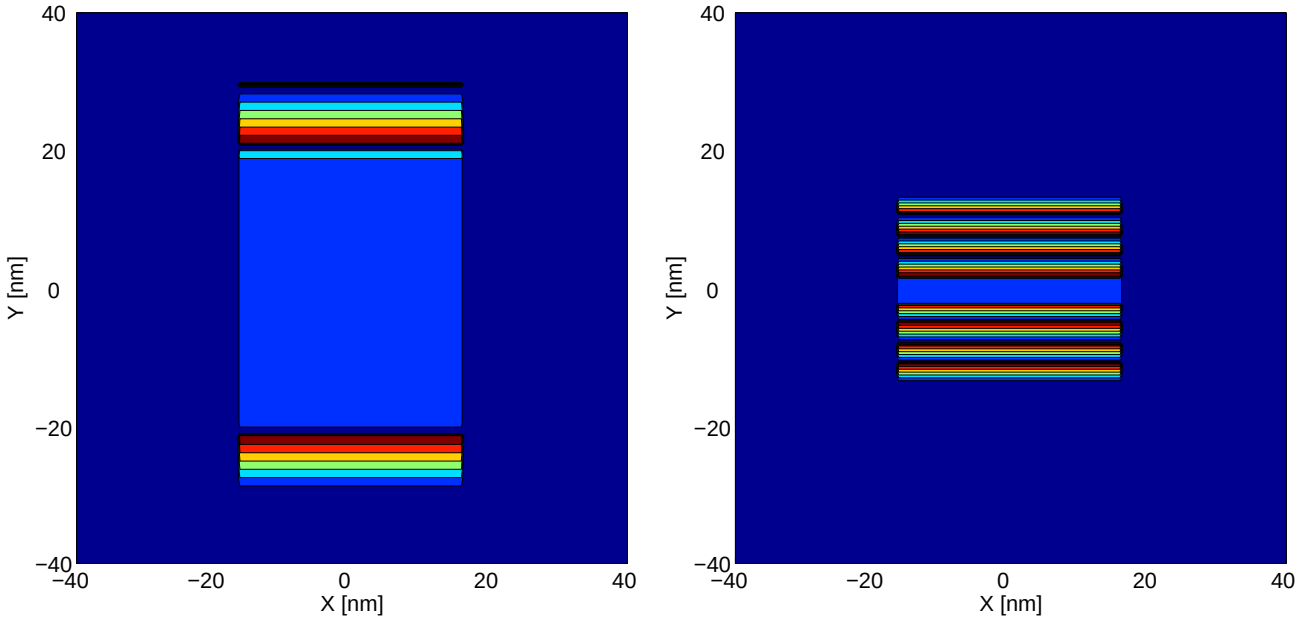

FIG. 19: Electric contribution ϕ_e to the phase ϕ (amplified 8 times) for a slab of dimensions $L_x = 32\,\text{nm}$, $L_y = 64\,\text{nm}$, and $L_z = 16\,\text{nm}$, using an inner potential $V_0 = 1\,\text{V}$, and 200 kV electrons: (a) $\theta = 40°$; (b) $\theta = 80°$.

[3] J. Cowley, Ultramicroscopy **41**, 335 (1992).
[4] P.A. Midgley, P.A., *An Introduction To Off-axis Electron Holography*, Micron **32**, 167 (2001)
[5] T. Vystavel, S.A. Koch, G. Palasantzas, J.Th.M De Hosson, Applied Physics Letters **86** , 113113 (2005).
[6] J. Li, M.R. McCartney, D.J. Smith, Ultramicroscopy **94**, 149 (2003).
[7] E. Völkl, F. Allard and D.C. Joy, *Introduction to Electron Holography*, Kluwer Academic/Plenum Publishers, ISBN 0-306-44920-X (1999).
[8] G. Baym, *"Lectures in Quantum Mechanics"*, W.A. Benjamin MA (1974).
[9] Y. Aharanov and D. Bohm, Phys. Rev. **115**, 485 (1959).
[10] A. Tonomura, Rev. Mod. Phys. **59**, 639 (1987).
[11] J.D. Jackson, *Classical Electrodynamics*, Wiley (1998).
[12] M. Beleggia and G. Pozzi, Ultramicroscopy **84**, 171 (2000).
[13] M. Beleggia, P.F. Fazzini, and G. Pozzi, Ultramicroscopy **96**, 93 (2003).
[14] M. Beleggia and Y. Zhu, Phil. Mag. **83**, 1045(2003).
[15] M. Beleggia, Y. Zhu, S.Tandon and M. De Graef, *Electron-optical phase shift of magnetic nanoparticles II. Polyhedral particles*, Phil. Mag. **83**, 1143(2003).
[16] W.H. Press, S.A. Teukolsky, W.T. Vetterling and B.P. Flannery, *Numerical recipes in Fortran 77 (Second edition)*, url: `http://www.numerical-recipes.com/`
[17] G. Palasantzas, Phys. Rev. B **48**, 14472 (1993).
[18] J.TH.M. de Hosson, H.A. de Raedt, Rev. Adv. Mater. Sci. **5**, 403 (2003).
[19] H.B. Braun, Phys. Rev. B **50**, 16485 (1994).
[20] M. De Graef, N. T. Nuhfer and M. R. McCartney, J. Microsc. **194**, 84 (1999).
[21] D. Gabor, Nature (London) **161**, 777 (1948).
[22] I.S. Gradshteyn and I.M. Ryzhik, *Table of Integrals, Series, and Products 4th Edition*, Academic Press (1965).
[23] M. Abramowitz and I. A. Stegun, *Handbook of Mathematical Functions*, Dover Publications (1965).